PCCP

PAPER

View Article Online
View Journal | View Issue

Cite this: *Phys. Chem. Chem. Phys.*, 2025, **27**, 22187

Kinematic and thermodynamic studies on water micro-droplets supercooled in a vacuum

Takefumi Handa, Masashi Arakawa, † Masato Yamaguchi, ‡ Takuya Horio and Akira Terasaki *

Evaporation of water droplets in a vacuum induces rapid evaporative cooling that leads to a supercooled state of water. Observation of supercooled water provides valuable insights into ice nucleation and subsequent freezing processes. Here, we introduce 40 μm water droplets into a vacuum to study their cooling and freezing dynamics by several experimental techniques. High-speed imaging is employed to observe oscillatory distortion that reflects surface tension and viscosity of the supercooled droplets and to capture fragmentation of freezing droplets. Observation of whispering gallery modes in the OH stretching Raman band enables precise measurement of the droplet size in the course of evaporation. Furthermore, a freezing curve, *i.e.*, a fraction of frozen droplets as a function of time, is measured by capturing laser-scattering images to discriminate between frozen and unfrozen droplets. The experimental approaches to the evaporation rate and subsequent freezing time, along with thermodynamics simulations based on the Knudsen theory, allow us to determine homogeneous ice nucleation rates between 232 and 235 K.

Received 15th June 2025,
Accepted 20th September 2025

DOI: 10.1039/d5cp02281a

rsc.li/pccp

1. Introduction

Evaporation of water droplets in a vacuum shows significantly different behavior compared with that in the air. Free evaporation induces rapid evaporative cooling as the evaporating water molecules carry heat away from the droplet without condensation back to the liquid phase. Such fast evaporative cooling offers an opportunity to investigate supercooled water. The temperature of such water droplets with sizes in the 10 μm range is reported to be 250 K as estimated using the conventional Knudsen kinetic model[1–5] and even reaches 230 K as evaluated by Raman thermometry.[2,5] Pure water can retain the liquid phase at temperatures far below its normal melting point.

The freezing process of water is either heterogeneous or homogeneous. When the droplet is as small as 50 μm in diameter, which is only 65 pL in volume, homogeneous ice nucleation dominates the process due to a negligible number of heterogeneous nucleation sites in such a small volume. Therefore, micrometer-sized water droplets in a vacuum are suitable to investigate supercooled water and homogeneous ice nucleation. Formation of homogeneous ice nuclei is not limited to laboratory measurements; it also occurs in cloud droplets that are transported to high altitudes.[6,7] The temperatures of supercooled water ranging from −38 to −35 °C reported for clouds as observed by *in situ* measurements are consistent with the lowest temperatures of supercooled water droplets, with a size of 10 to 100 μm, reported from laboratory experiments.[8]

The freezing process of supercooled water droplets starts from a dendritic growth phase for both homogeneous[9] and heterogeneous[10,11] ice nucleation. An experimental study has even been conducted to investigate the size of the critical ice nucleus required for freezing.[12] After ice nucleation, ice formation proceeds until the latent heat released by crystallization increases the droplet temperature to its melting point. During the early stage of freezing, it has been reported that water droplets travelling at a constant velocity are deflected spontaneously.[5] This deflection is attributed to the release of the latent heat, which induces localized evaporation.[9] The hydrogen-bond network structure of supercooled water near the temperature of homogeneous ice nucleation differs from that of water at room temperature, suggesting a tetrahedral ordering as observed by diffraction of femtosecond X-ray laser pulses.[3] Heterogeneous freezing of supercooled water droplets at an atmospheric pressure was studied by laboratory measurements, where fragmentation is reported for droplets with diameters of a few tens to hundreds of micrometers.[11,13] To the best of our knowledge, there is one report on fragmentation upon homogeneous freezing;[14] however, the details of the process remain unclear.

Due to the difficulty in accessing the supercooled regime, the homogeneous ice nucleation rate is a topic that has been continuously attracting attention in experimental research.

Department of Chemistry, Faculty of Science, Kyushu University, 744 Motooka, Nishi-ku, Fukuoka, 819-0395, Japan. E-mail: terasaki@chem.kyushu-univ.jp
† Present address: Department of Earth and Planetary Sciences, Faculty of Science, Kyushu University, 744 Motooka, Nishi-ku, Fukuoka 819-0395, Japan.
‡ Present address: Department of Basic Science, Graduate School of Arts and Sciences, The University of Tokyo, Komaba, Meguro-ku, Tokyo 153-8902, Japan.

The ice nucleation rate is expected to increase as the temperature decreases. Most of the experiments on homogeneous ice nucleation have employed micro-meter sized droplets under an atmospheric pressure to reach temperatures between ~235 and ~240 K.[15–19] Droplets in the nanometer size range have been shown to offer even lower ice nucleation rates and higher cooling rates, reaching temperatures between ~195 and 225 K.[20–23] At the intermediate temperatures, micro-meter droplets in a vacuum serve an appropriate opportunity, *e.g.*, volume-based homogeneous ice-nucleation rates (J_V), in the range between 228 and 233 K are reported by Hagen *et al.*[24] and Laksmono *et al.*[25] although their J_V values are significantly different from each other. As for the temperature range between 233 and 235 K, it has been reported that heterogeneous nucleation, induced by the droplet surface, dominates the freezing process at a cooling rate of 0.25 K s^{-1} or slower;[26] our vacuum-based experiment, enabling exceptionally rapid cooling exceeding 10^3 K s^{-1}, is anticipated to allow access to homogeneous freezing even in this temperature range.

In the present study, water droplets with a diameter of about 40 μm are introduced from a piezo-driven nozzle into a vacuum to explore the sequence of their dynamics. The exploration reveals the physical and thermodynamic properties of supercooled water, including the surface tension, viscosity, evaporation rates and homogeneous ice nucleation rates, which are not readily accessible by other approaches. The following sequence of events is investigated: (1) a quadrupolar oscillation of the droplet, which is excited upon detachment from bulk water during its formation, is recorded using a high-speed camera. The deformation dynamics enables us to derive the surface tension and viscosity of the droplet. (2) The evaporation rate of the droplet is evaluated by the measurement of the droplet size as a function of time *via* the frequency shifts in the whispering gallery modes (WGMs) of cavity enhanced Raman scattering on a single-laser-shot basis. The evaporative cooling rate calculated from the time-dependent droplet size is compared with that obtained computationally by the Knudsen theory. (3) Subsequent ice formation is probed by imaging light of a continuous-wave (cw) laser scattered at the right angle from the droplet, where the droplet temperature is specified by the distance from the nozzle exit. The freezing time, *i.e.*, time elapsed after droplet generation until freezing, of each droplet gives us homogeneous ice-nucleation rates between 232 and 235 K that fill the gap between the J_V data reported for the lower temperature range by Hagen *et al.*[24] and Laksmono *et al.*[25] and those of the higher temperature range measured for micro-droplets at various ambient pressures.[15,17,19] (4) A series of phenomena upon freezing, such as spicule formation and fragmentation, are captured using a high-speed camera to discuss the freezing dynamics.

2. Experimental

2.1. Droplet generation

The procedure for generating droplets of pure water in a vacuum is described below. The setup is shown in Fig. 1; we improved the one previously reported[4,27,28] due to the requirement of sufficiently stable droplet generation for precise measurements of size by employing the WGM. The chamber was evacuated using a dry vacuum pump, where the pressure was maintained at 1 to 5 Pa. Droplets were generated using a piezo-driven nozzle (MD-K-130, microdrop Technology GmbH). Distilled water (Wako Pure Chemical Industries, Ltd) was used for the sample preparation. A polyvinylidene difluoride (PVDF) membrane filter (5 μm pore size) was employed for particle removal from the sample water to avoid clogging in the nozzle, which is the most serious issue that could disturb droplet generation. The filtration is also intended to make the water sample free from particles that might act as heterogeneous nuclei. If some of the droplets were contaminated with particulates, such droplets would show separate nucleation statistics within the ensemble of pure droplets. The dispenser head operates based on the principle of ink-jet printing technology. The pathway from the reservoir to the nozzle was cooled by ice for suppressing bubble formation inside the tube, enabling stable water droplet generation. The core of the dispenser head consists of a glass capillary with an inner diameter of 30 μm and a tubular piezo actuator surrounding the capillary. The droplet size was adjustable in the range of 35–50 μm in diameter (corresponding to 22–65 pL) by tuning the duration and amplitude of the pulsed voltage applied to the piezo actuator.

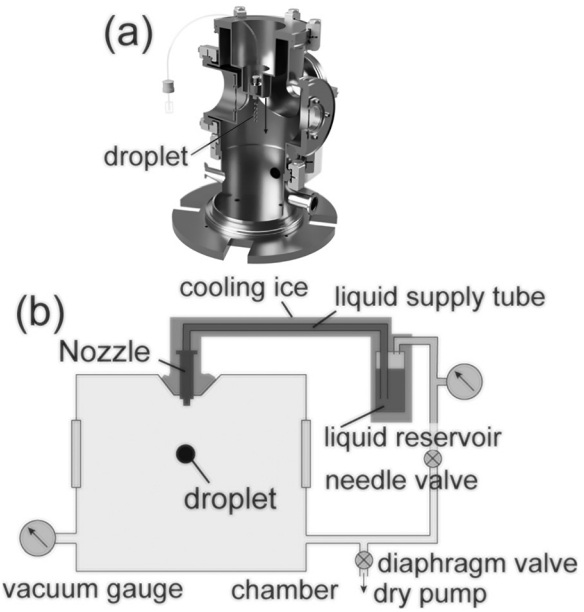

Fig. 1 (a) A rendered view of the system for droplet generation in a vacuum. (b) A schematic view of the setup.

2.2. Quadrupolar vibration

Oscillation of micro-droplets was captured *via* high speed imaging (ACS-1, nac Image Technology Inc.). The shape descriptors calculated in this study are the diameter, an aspect ratio and roundness. Among these, the aspect ratio is preferable, which minimizes the influence of the depth-of-field effect in capturing the vibration of water droplets. The image was

taken at a rate of 400 kHz, an image size of 1280 × 96 and an exposure time of 1 μs, from which an aspect ratio was calculated by elliptical fitting of the contour of the image to extract the lengths of the longer and shorter axes. Measurements were conducted for 42 μm droplets both in the atmosphere and in a vacuum. The experiment at an ambient pressure was conducted under water–vapor saturation to prevent droplet evaporation.

2.3. Droplet-size measurement

The droplet diameter was measured using WGMs as a function of time. The experimental setup is shown in Fig. S1 (SI). Generation of droplets, excitation by laser pulses and acquisition of the Raman spectrum were synchronized to TTL pulses from a digital delay generator (DG645, Stanford Research Systems) at a repetition rate of 5 Hz. WGM spectra were obtained shot-to-shot (see Fig. S2 of the SI) as a function of time elapsed after droplet generation (100–4000 μs). For excitation, a linearly polarized pulsed laser at a wavelength of 532.05 nm emitted from second harmonics of a Q-switched Nd:YAG laser (VM-2134UTF, VM-TIM GmbH) was focused on the droplet edge. The spot size at the droplet was adjusted to 30 μm in diameter. The pulse energy was adjusted to be below 180 μJ. Raman scattering was collected using a telecentric objective lens (ML × 10, Mitutoyo Corp., NA: 0.21, working distance: 51 mm). A homemade microscope system was created to combine the objective lens with a camera and a spectrometer (customized YSM-8102-06 series, YIXIST).

The WGM wavelengths and the free spectral range (FSR) were obtained through Gaussian fitting of the spectra. The droplet size is calculated from WGM resonances based on the dispersion equation:[29,30]

$$\frac{1}{j_l(\rho_1)}\frac{\partial[\rho_1 j_l(\rho_1)]}{\partial\rho_1} = \frac{b}{h_l^{(1)}(\rho_2)}\frac{\partial\left[\rho_2 h_l^{(1)}(\rho_2)\right]}{\partial\rho_2} \quad (1)$$

Here, $j_l(\rho_1)$ is the spherical Bessel function, $h_l^{(1)}(\rho_2)$ is the spherical Hankel function, subscript l is the angular mode number and $\rho_i = \pi d n_i/\lambda_0$ ($i = 1, 2$) is the size parameter, where n_i is the refractive index (the subscripts 1 and 2 denote vacuum and water, respectively), λ_0 is the wavelength of light in a vacuum and d is the diameter of the sphere. Parameter b is the polarization dependent factor that is μ_2/μ_1 for TE modes and $\mu_2 {n_1}^2/\mu_1 {n_2}^2$ for TM modes. The observed WGM resonances (Fig. S2 of the SI) belong almost to a single radial mode. The radial-mode number is reported to increase from 1 to 2, when the droplet size becomes larger from 10 to 50 μm;[31] it was assigned a value of 2 in this study by referring to ref. 29. As for the polarization of WGMs, the TE mode was selectively measured (Fig. S3 and S4 of the SI). The temperature dependence of the refractive index was taken into account based on the cooling rate estimated using the Knudsen equation,[4,32] which employs the given initial diameter and the initial temperature measured at the nozzle. The temperature of the droplet surface was employed because the present measurement is a surface-sensitive technique due to the WGMs representing successive internal total reflection near the surface of the microcavity in the ray-optics approximation. The temperatures measured *via* Raman OH stretching bands and those simulated by the Knudsen model agree well with each other, as has been reported previously.[1,2] For dispersion of the refractive index, the four-term Sellmeier dispersion formula at 297.0 K[33] was extrapolated to supercooled water. Without accounting for dispersion, the deviation in the droplet size is estimated to be +0.50 μm with respect to that with dispersion.

2.4. Imaging Mie scattering for identifying freezing

The time of ice nucleation is recorded by observing Mie scattering images. The images were detected with a CMOS camera (IMX-249, Sony Group Corp.) placed at the right angle to the illumination of a CW laser at 532 nm (spot size: 1 mm). The field of view of the camera mounted with a telecentric objective lens 3× (Mitutoyo Corp.) was 1 mm × 0.8 mm. The flight time of a droplet was measured by superimposing a bright field image captured with a 5 μs strobe LED synchronized with the trigger to the nozzle. The exposure time is sufficiently longer than 1 ms, which is the duration for a water droplet to pass through the field of view.

A typical image is shown in Fig. 2. The recorded images were classified into three categories based on the Mie scattering and the bright-field image of the droplets: intact liquid droplets, ice-containing droplets and missing droplets (mainly due to droplets moving out of the field of view). Liquid/solid classification was performed as follows: the time elapsed after droplet generation was recorded by the bright-field image observed using the strobe LED. If the position of freezing, as identified by brightening of the stream in the Mie-scattering image, was closer to the nozzle than the position of the bright-field image, as shown in Fig. 2, the droplet was classified as ice-containing

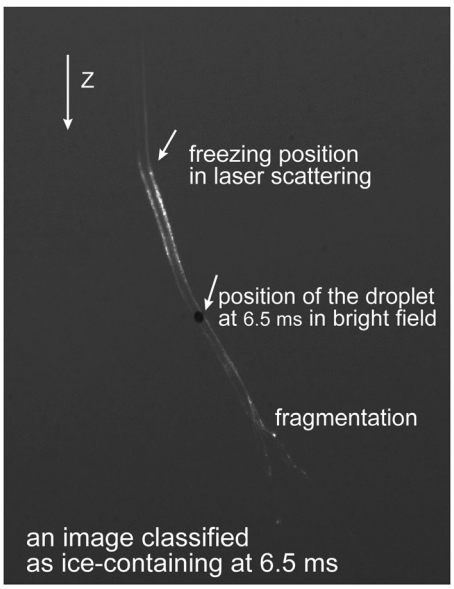

Fig. 2 A right-angle light scattering image of a water droplet (40 μm) by irradiating a CW laser, which is superimposed with a bright-field image at t = 6.5 ms by illuminating the droplet using a strobe LED.

at that time. Time-dependent liquid-to-solid phase transition was thus tracked.

These processes of classification were automated *via* machine learning. Automation through deep learning uses transfer learning from a pre-trained convolution neural network (CNN). By considering the trade-off between accuracy and speed in the CNN, the Inception-v3 model[34] was employed. For training data sets, we prepared 9100 images. Categorized 3900 images were used to evaluate the CNN models after transfer learning. The training cycle was set to 8 epochs and 64 iterations. Visual inspection of the classified images is performed in the final stage. The method described above is consistent with the results obtained using a technique that investigated the polarization state of droplet scattering.[4,17]

2.5. High-speed imaging for observing the droplet morphology

The freezing process was visualized with a microscope (Z16 APO with a 1× objective lens and an additional 2.5× zoom). A high-speed camera recorded movies of the droplets at a given time delay, t, from droplet generation, which was triggered using a digital delay generator. The typical frame rate was set to 54 kHz. For supporting the high frame rate and a large field of view, images were acquired using a bilinear-based interpolation method. The field of view achieved with this setup was 800 μm × 1200 μm.

3. Results and discussion

3.1. Oscillation of water droplets

During droplet generation, a water droplet gains a surface energy upon separating from bulk water.[35] The deformation of the droplets can be captured as a quadrupolar oscillation through measurement of an aspect ratio using high-speed imaging. As the deformation dynamics is governed by surface tension and viscosity of the droplet, it enables contactless measurement of these physical constants. The conventional physical models linked to these material properties are the Rayleigh and Lamb formulae;[36,37] both equations are derived under weakly damped oscillations. The model has been extended to large-amplitude oscillations,[38,39] which is applicable in the present case showing deformation with a large aspect ratio (>1.2). In this study, surface tension γ and viscosity η were calculated based on the basic characteristic equation of the linear Navier–Stokes equation introduced by Lohöfer, which represents a model applicable to any damping range:[39]

$$\gamma = \frac{3M}{32\pi}{\omega_2}^2 \tag{2}$$

$$\frac{1}{\eta} = \frac{20\pi a}{3M}\tau_2\left(1 - \sqrt{\frac{18}{125}}\frac{1}{\sqrt{\omega_2\tau_2}}\right) \tag{3}$$

where ω_2 and τ_2 are the oscillation frequency and the damping time constant of the fundamental quadrupolar mode l = 2, respectively, M is the droplet mass and a is the equilibrium radius of the droplet. Oscillatory deformation of a liquid droplet around the equilibrium point can be described by the second-order spherical harmonics. The radius r changes as a function of time t and polar angle θ as

$$r(t,\theta) = r_0\left[1 + \frac{1}{2}A_2(t)\left(3\cos^2\theta - 1\right)\right] \tag{4}$$

where $A_2(t)$ is an instantaneous amplitude of the 2nd oscillation mode normalized by the initial radius r_0. $A_2(t)$ is expressed by the aspect ratio ξ as follows:

$$A_2(t) = \frac{\xi(t) - 1}{1 + \xi(t)/2} \tag{5}$$

ω_2 and τ_2 can be extracted from the time evolution of A_2 and its Fourier transform.

We measured quadrupolar oscillation both at an atmospheric pressure and in a vacuum. Fig. 3 shows the aspect ratio of water droplets as a function of time. Since the droplets were found to rotate in air with an angular velocity of 0.83° s^{-1},[40–42] this effect was taken into account in the estimation of the aspect ratio; inclination from the image plane and rotation about the z-axis were ignored. The values of surface tension and viscosity in air calculated from eqn (2) and (3) were 76.0 mN m^{-1} and 1.22 mPa s, respectively, where the ω_2 of 2.53×10^5 s^{-1} and the τ_2 of 8.03×10^{-5} s were derived from the data fitting, the droplet radius of 21.2 μm was measured from the high-speed image and the density of water was adopted to be that for the nozzle temperature of 8.5 °C as measured. The present values of surface tension and viscosity are in reasonable agreement with the reference data, 74.37 mN m^{-1} and 1.356 mPa s, respectively, of water at 9 °C.[43]

Damping oscillation was also measured in a vacuum using the same method, as shown in Fig. 3. The oscillation is discernible up to 150 μs. According to temperature simulations based on the Knudsen theory, the mass averaged temperature of the droplet at 150 μs is 273 K (266 K at the surface), when the initial temperature and diameter are 280 K and 40 μm, respectively. The decrease in the mass averaged temperature

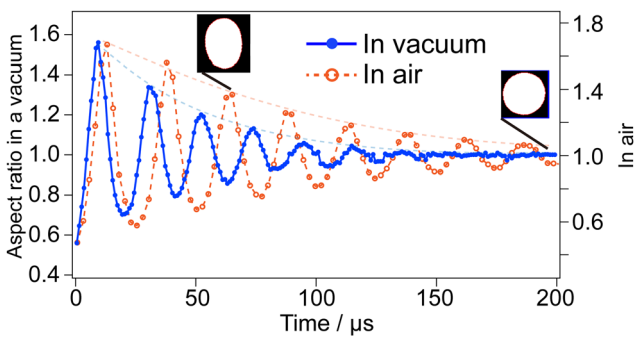

Fig. 3 Aspect ratio of the droplet as a function of time after the droplet left the nozzle in the atmosphere (dashed line) and in a vacuum (solid line) as measured by high speed imaging (400 kHz). The thin dashed lines show contours of the damping oscillations. Binary images show the shape of the droplets at 64 and 200 μs in the air. The aspect ratio takes into account an angular velocity of 0.83° s^{-1} estimated by elliptical fitting.

from 280 to 273 K leads to increases in the surface tension and viscosity from 74.7 to 75.7 mN m^{-1} (ref. 44) and from 1.425 to 1.794 mPa s,[45] respectively. Compared to the measurement at 8.5 °C in the atmosphere, the higher surface tension and viscosity at the lower temperature are attributed to a higher oscillation frequency and an increased damping rate, respectively.

3.2. Droplet evaporation as a function of time

The droplet diameter is shown in Fig. 4 as a function of time (100–4000 μs), which was evaluated using the procedure presented in Section 2.3. An oscillation in the droplet diameter, originating probably from the quadrupolar vibration, was observed just after its generation from the dispenser head up to about 900 μs. It was found that the measurement of WGMs is challenging for highly deformed droplets with aspect ratios far from unity; prolate droplets with a major axis longer by ~2 μm than the minor ones were not captured in the WGM measurements. The quadrupolar vibration of droplets was also observed in detail by measuring the aspect ratio using a high-speed camera as presented in Section 3.1. The linear fitting of the droplet size beyond 900 μs resulted in an evaporation rate of 0.21 ± 0.08 μm ms^{-1}. The simulated evaporation rate is shown by the green solid curve that was obtained using the Knudsen equation as described elsewhere.[4] The simulated evaporation rate between 900 and 3000 μs was 0.11 μm ms^{-1}, which is almost consistent with the experimental value although it is slightly less than the experimental lower bound. Note that the amplitude of the quadrupolar vibration can be negligible in the measurement of the diameter in the time range beyond 900 μs (see Fig. S5 of the SI).

3.3. Homogeneous ice-nucleation rate of water

Ice formation in a vacuum due to homogeneous ice nucleation has been reported by state-of-the-art experiments employing OH-band Raman spectroscopy,[5] X-ray spectroscopy[3] and laser scattering.[4] The homogeneous ice formation is a stochastic process, where the ice nucleation rate increases rapidly as the temperature decreases below the homogeneous-ice-nucleation temperature.[3,4] Homogeneous ice nucleation rates are reported in an ambient gas[46] and in inverse (water-in-oil) emulsions[18] as well.

The volume-based homogeneous ice-nucleation rate (J_V) was calculated from the frozen fraction f_{ice} of droplets as demonstrated in other nucleation studies.[4,15,22,25] The probability $P_x(\Delta t)$, where x-times of ice-nucleation events occur in a droplet with a volume V during a time interval Δt, can be expressed by the following Poisson distribution:

$$P_x(\Delta t) = \frac{(J_v(T)V\Delta t)^x}{x!}\exp[-J_v(T)V\Delta t] \quad (6)$$

where T is the given temperature. On the premise that a droplet starts freezing immediately after ice-nucleus formation, we may replace $P_{x=0}(\Delta t)$ by $1 - f_{ice}(\Delta t)$. The equation for the frozen fraction f_{ice} can be rearranged as an equation for time dependence of J_V:

$$J_V(t_n) = \frac{\ln[(1 - f_{ice}(t_n))/(1 - f_{ice}(t_{n+1}))]}{V_{droplet} \times (t_{n+1} - t_n)} \quad (7)$$

where $V_{droplet}$ is the droplet volume and subscripts n and $n + 1$ represent successive measurements.

The experiment was conducted for 39.4 μm water droplets generated in a vacuum. The fraction of ice-containing droplets increased as a function of time elapsed after droplet generation. The fraction of ice-containing droplets thus measured as a function of time is shown in Fig. 5. The fraction of ice-containing droplets rapidly increased within 1300 μs. The estimation of the temperature was based on the Knudsen theory of evaporative cooling applied to a droplet initially at the nozzle temperature (280.5 K). Note that a slight change in the initial temperature has only a negligible effect on the temperature estimation in the vicinity of homogeneous ice nucleation; this is due to the high evaporative cooling rate,

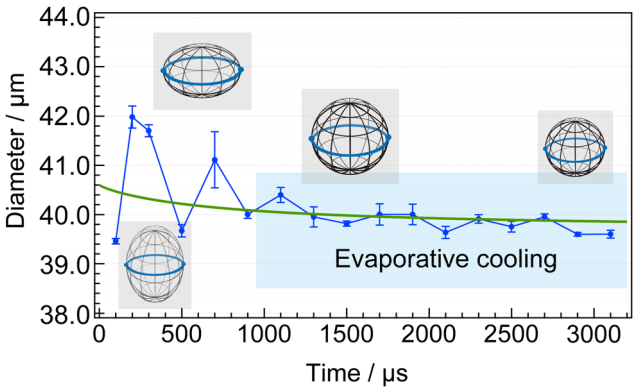

Fig. 4 Droplet size as a function of time. The blue circles show experimental data of the diameter determined from the whispering gallery modes in the Raman OH band. The error bars represent standard errors. The green solid curve shows prediction by the Knudsen evaporation model with an evaporation coefficient of unity, where the initial conditions of the diameter and the temperature were assumed to be 40.6 μm and 280.45 K, respectively.

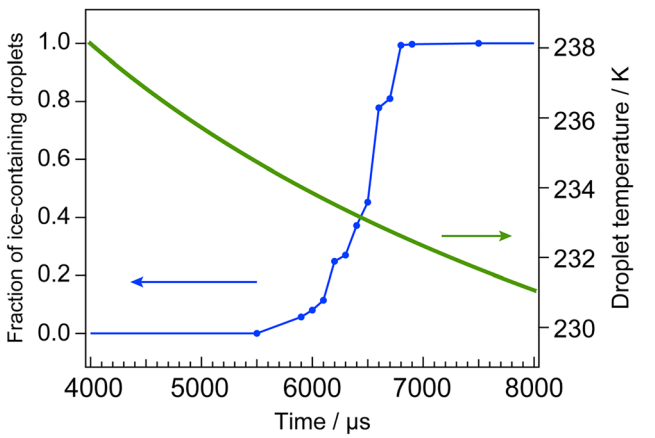

Fig. 5 The fraction of ice-containing droplets as a function of time in a vacuum for water droplets with an initial diameter of 39.4 μm. The droplet temperature was simulated by the Knudsen theory of evaporation.

which is estimated as high as 1.8×10^3 K s^{-1} indeed, and also due to the fact that a higher initial temperature leads to an increase in the vapor pressure and thus faster cooling in the beginning. On the other hand, to deal with the effect of the thermal conduction, a model droplet is divided into 100 spherical shells. Such a shell model is often used for analysis of thermal conductance in water droplets.[2,4,10] The details of the model were described elsewhere.[4] The vapor pressure and vaporization enthalpy were calculated by using the equations proposed by Murphy and Koop,[47] which were derived from the exponential fit to the data of C_p measured by Archer and Carter.[48] The density was calculated by using the sixth-order polynomial reported by Hare and Sorensen.[49] The thermal conductivity κ was calculated by using the equation proposed by the International Association for the Properties of Water and Steam (IAPWS).[50] Although an evaporation coefficient is under debate, we assumed a value of unity here.[4,51]

The ice nucleation rates obtained from eqn (7) range from 2.1×10^9 to 4.8×10^{11} cm^{-3} s^{-1} as the temperature decreases from 235 to 232 K (red triangles in Fig. 6). For the temperature of the droplet, a mass-averaged temperature, $T_{ave} = \sum_{n=0}^{99} [T_n V_n \rho(T_n)]/m$, was employed ($\rho$ and m are the density of water and the mass of the droplet, respectively). The error in the temperature accounts for the temperature gradient inside the droplet; the temperature is lower at the droplet surface, where evaporative cooling takes place. The ice nucleation most likely occurs in the vicinity of the surface, which is slightly colder than the inner part, because the nucleation rate shows a rapid increase with decreasing temperature. Furthermore, the volume of the shell decreases toward the center. About 95% of the ice-nucleation events occur in the region within 28% of the radius beneath the surface of 40 μm droplets, according to the shell model calculations taking into account the gradient in the temperature. Therefore, the mass averaged temperature calculated for the outer region from the 72nd to 100th shells is also shown by blue circles in Fig. 6. We hereafter discuss the homogeneous ice nucleation rate at the outer-region temperature near the surface.

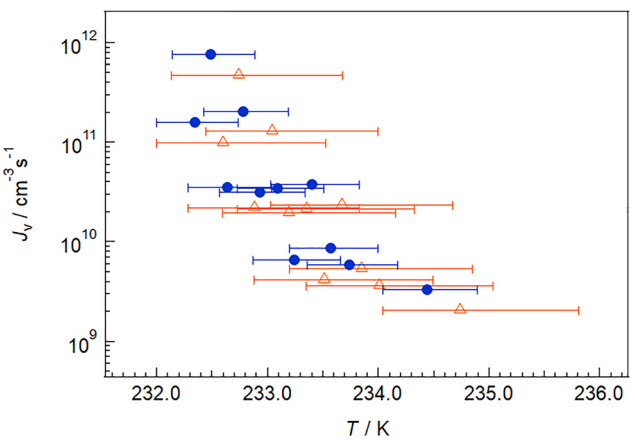

Fig. 6 Volume-based homogeneous ice-nucleation-rate coefficients J_V measured as a function of temperature within 232–236 K. The error bars account for the temperature gradient inside the droplet. Triangles (red) show the mass averaged temperature calculated over the shells from the 1st (center) to 100th (surface); the upper/lower limit indicates the temperature of the center/surface of the droplet. Circles (blue) show those calculated over the shells from the 72nd to the 100th; the upper/lower limit indicates the temperature of the 72nd shell/surface (100th shell). Note that the J_V values are evaluated by taking into account the corresponding different volumes for the two cases.

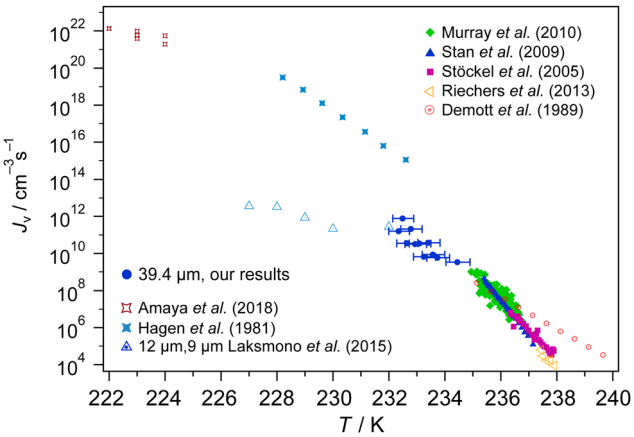

Fig. 7 Volume-based homogeneous ice-nucleation-rate coefficients Jv measured as a function of temperature from 222 to 240 K.

Finally, we show the $J_V(T)$ values derived here (blue circles in Fig. 6) together with literature values from previous experimental studies in Fig. 7. The present J_V values are close to extrapolation of the values reported for 235–238 K, especially those in the study by Stöckel *et al.* The values reported for temperatures below 232 K show discrepancies between the data presented by Laksmono[25] and Hagen *et al.*[24] Nonetheless, our values tend to align more closely with the values in the study by Laskmono *et al.*[25] Since their data were obtained under similar conditions of evaporative cooling of ~10 μm droplets, the agreement with our data is not surprising.

3.4. Freezing process and fragmentation of droplets

Typical sets of images of homogeneously frozen pure water droplets are shown in Fig. 8, where the droplets are recorded at 148 μs intervals. The irregular stream of droplet images (Fig. 8a) indicates that the freezing droplets undergo deceleration and acceleration. A droplet should retain its initial velocity in a vacuum because the effect of gravity is negligible in the present case. Therefore, the change in its velocity indicates an effect originating from evaporation of the droplet itself. This is shown in the trajectory of a droplet reported by Ando *et al.*[4] and in an image of a spreading train of droplets reported by Stan *et al.*[9] The model by Stan *et al.* predicts the presence of a mixture of liquid and ice on the droplet surface during the freezing stage, which results in asymmetric evaporation due to the difference in the evaporation rates of ice and water, thereby accelerating the droplet. Such a behavior is displayed in Fig. 8b as well, where significant deflection in the trajectory is observed at 6.4 ms and later up to 7.2 ms.

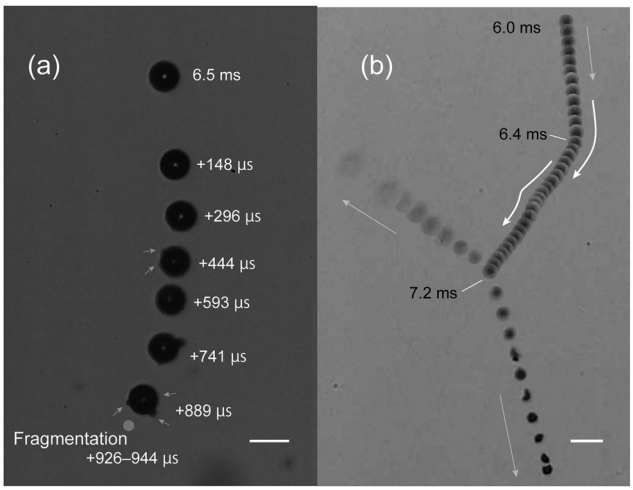

Fig. 8 High-speed microscopy images of freezing water droplets in a vacuum. (a) Ice spicules are captured at around 6.9 ms (the image taken at +444 μs from 6.5 ms). The magnification was set to ×23 (scale bar: 50 μm). (b) Spontaneous trajectory deflection and subsequent fragmentation were observed. The magnification was ×6.25 (scale bar: 100 μm).

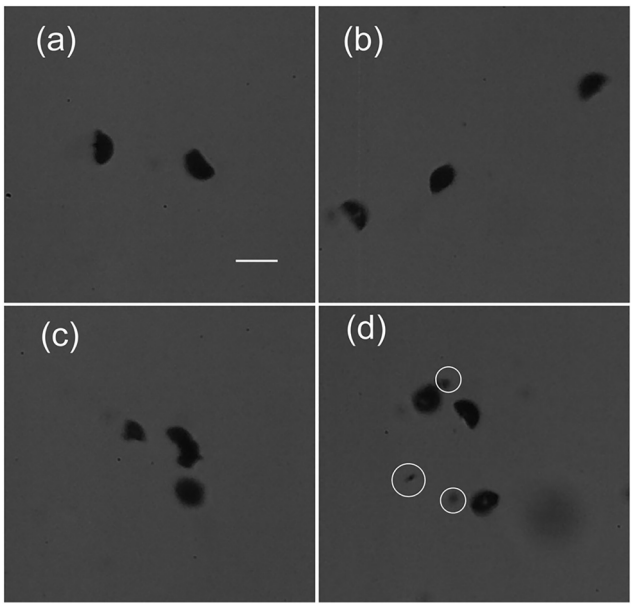

Fig. 9 Fragmentation of water droplets (scale bar: 50 μm). (a) Most of the droplets break up into two fragments. In some cases, (b) three and (c) four fragments were observed. (d) Occasionally, additional small fragments were observed.

We also point out that ice spicules are observed at 6.9 ms (arrows in Fig. 8a), which grow up further; similar events were confirmed in almost all of the droplets examined. The spicules have been reported both at an ambient pressure and in a vacuum during the freezing stage of supercooled droplets.[46,52,53] High speed recording by Wildeman *et al.* showed that the spicules were formed upon freezing of inner water, which was squeezed out of the outer ice shell through cracks.[53] Formation of an ice shell has been observed after dendritic ice growth.[14,53,54] It is noteworthy that images of 50 μm frozen droplets are reported to show the presence of spicules in homogeneous freezing, whereas heterogeneous ice nucleation at −8 °C of the same size shows no spicules or deformation.[46] In other studies, spicule formation is also reported for heterogeneous freezing,[53] where droplets freeze into polycrystalline ice; spicules are formed with a probability of 90–100% in this case.[55,56]

Furthermore, we would like to point out that the present 40 μm droplet shown in Fig. 8b eventually fragments into two parts at 7.2 ms; one should note that fragmentation of droplets smaller than 50 μm has not been reported previously under an atmospheric pressure.[46,57,58] From the simple theoretical model of kinetic-energy balance, Wildeman *et al.*[53] predicted that symmetrically freezing droplets smaller than 100 μm in diameter cannot break up. In contrast to this prediction, fragmentation of ice droplets as small as 42 μm was observed for most of the droplets examined in the present study. Fig. 9 shows four more images of fragmentation events. It was observed that, out of 128 freezing events, 85% of droplets break up within the field of view. Since the flight trajectories of the droplets change their direction after ice nucleation, a broad field of view (3.1 × 4.5 mm) ensures the validity of the experiment. These events include 73% of splitting into approximately two equal fragments, 10% into three and 2% into four. Recently, Kalita *et al.*[14] also captured the fragmentation of 40 μm droplets. They measured the probability of fragmentation to be 60%.

The mean fragmentation time (time elapsed from ice nucleation to fragmentation) is estimated to be 610 ± 100 μs, which is derived by assessing the time interval between the first kink of the trajectory and the onset of fragmentation. From the laser scattering pattern as shown in Fig. 2, the onset of freezing coincides with the irregular deflection of the trajectory. The fragmentation time from ice nucleation is predicted to be 10 ms[53] for 50 μm droplets, which is more than 10 times longer than the present observation (610 μs) for 40 μm droplets. The model calculation[53] assumes that the increase in the internal pressure is occasionally released by multiple cracks. In contrast, in the present study in a vacuum, the 3 rates of an ice shell may have exceeded the pressure release through cracking due to ice nucleation following rapid evaporative cooling.

4. Summary

We investigated 40 μm pure water droplets introduced into a vacuum to study evaporative cooling and freezing dynamics of supercooled water. The major findings are as follows: (1) the quadrupolar oscillation excited upon droplet generation manifested increases in the surface tension and viscosity in the supercooled state. (2) The size of evaporating water droplets was probed *via* WGMs observed in the OH stretching band of their Raman scattering spectrum. The evaporation rate measured *via* time evolution of the droplet diameter was −0.21 ± 0.08 μm ms^{-1}. (3) In the subsequent freezing process, volume-based homogeneous ice-nucleation rates (J_V) were evaluated from Mie-scattering images, which were analyzed by a

computational approach assisted by machine learning; the temperatures were estimated by the Knudsen theory. The ice-nucleation rates thus evaluated exhibited a significant increase from 2.1×10^9 to 4.8×10^{11} cm^{-3} s^{-1} in the temperature range of 235 to 232 K. (4) Freezing droplets formed spicules on their surface, and eventually 85% of the 42 μm droplets were found to undergo fragmentation. These findings of the present study on the droplets of supercooled water may help improve the model of cooling and freezing processes of water.

Author contributions

THa contributed to methodology, investigation, software, formal analysis, data curation, visualization and writing – original draft; MA contributed to methodology, resources and writing – review and editing; MY and THo contributed to methodology and writing – review and editing; AT contributed to conceptualization, writing – review and editing, supervision, project administration and funding acquisition.

Conflicts of interest

There are no conflicts of interest to declare.

Data availability

The data supporting the findings of this study are available within the article and its supplementary information (SI). Supplementary information: A setup for the Raman spectroscopy; a spectrum of Raman WGMs; images of Raman WGMs; schematic views of WGMs propagating in the droplet; simulation of an evaporating droplet that shows damping oscillation. See DOI: **https://doi.org/10.1039/d5cp02281a**.

Acknowledgements

This work was supported financially by the Japan Society for the Promotion of Science (JSPS) KAKENHI [grant numbers JP21J21716, JP17H06456, JP21K18604 and JP23K17349]. The authors thank Yuta Suzuki for his valuable discussion on the thermodynamics of the droplets.

References

1 M. Faubel, S. Schlemmer and J. P. Toennies, *Z. Phys. D:At., Mol. Clusters*, 1988, **10**, 269.
2 J. D. Smith, C. D. Cappa, W. S. Drisdell, R. C. Cohen and R. J. Saykally, *J. Am. Chem. Soc.*, 2006, **128**, 12892.
3 J. A. Sellberg, C. Huang, T. A. McQueen, N. D. Loh, H. Laksmono, D. Schlesinger, R. G. Sierra, D. Nordlund, C. Y. Hampton, D. Starodub, D. P. Deponte, M. Beye, C. Chen, A. V. Martin, A. Barty, K. T. Wikfeldt, T. M. Weiss, C. Caronna, J. Feldkamp, L. B. Skinner, M. M. Seibert, M. Messerschmidt, G. J. Williams, S. Boutet, L. G. M. Pettersson, M. J. Bogan and A. Nilsson, *Nature*, 2014, **510**, 381.
4 K. Ando, M. Arakawa and A. Terasaki, *Phys. Chem. Chem. Phys.*, 2018, **20**, 28435.
5 C. Goy, M. A. C. Potenza, S. Dedera, M. Tomut, E. Guillerm, A. Kalinin, K. Voss, A. Schottelius, N. Petridis, A. Prosvetov, G. Tejeda, J. M. Fernández, C. Trautmann, F. Caupin, U. Glasmacher and R. E. Grisenti, *Phys. Rev. Lett.*, 2018, **120**, 015501.
6 A. J. Heymsfield and L. M. Miloshevich, *J. Atmos. Sci.*, 1993, **50**, 2335.
7 D. Rosenfeld and W. L. Woodley, *Nature*, 2000, **405**, 400.
8 H. R. Pruppacher, *J. Atmos. Sci.*, 1995, **52**, 1924.
9 C. A. Stan, A. Kalita, S. Marte, T. F. Kaldawi, P. R. Willmott and S. Boutet, *Phys. Rev. Fluids*, 2023, **8**, L021601.
10 T. Buttersack and S. Bauerecker, *J. Phys. Chem. B*, 2016, **120**, 504.
11 A. Lauber, A. Kiselev, T. Pander, P. Handmann and T. Leisner, *J. Atmos. Sci.*, 2018, **75**, 2815.
12 G. Bai, D. Gao, Z. Liu, X. Zhou and J. Wang, *Nature*, 2019, **576**, 437.
13 H. R. Pruppacher and R. J. Schlamp, *J. Geophys. Res.*, 1975, **80**, 380.
14 A. Kalita, M. M. McCourt, T. F. Kaldawi, P. R. Willmott, N. D. Loh, S. Marte, R. G. Sierra, H. Laksmono, J. E. Koglin, M. J. Hayes, R. H. Paul, S. A. H. Guillet, A. L. Aquila, M. Liang, S. Boutet and C. A. Stan, *Nature*, 2023, **620**, 557.
15 B. J. Murray, S. L. Broadley, T. W. Wilson, S. J. Bull, R. H. Wills, H. L. Christenson and E. J. Murray, *Phys. Chem. Chem. Phys.*, 2010, **12**, 10380.
16 C. A. Stan, G. F. Schneider, S. S. Shevkoplyas, M. Hashimoto, M. Ibanescu, B. J. Wiley and G. M. Whitesides, *Lab Chip*, 2009, **9**, 2293.
17 P. Stöckel, I. M. Weidinger, H. Baumgärtel and T. Leisner, *J. Phys. Chem. A*, 2005, **109**, 2540.
18 B. Riechers, F. Wittbracht, A. Hutten and T. Koop, *Phys. Chem. Chem. Phys.*, 2013, **15**, 5873.
19 P. J. Demott and D. C. Rogers, *J. Atmos. Sci.*, 1990, **47**, 1056.
20 J. Huang and L. S. Bartell, *J. Phys. Chem.*, 1995, **99**, 3924.
21 A. Manka, H. Pathak, S. Tanimura, J. Wolk, R. Strey and B. E. Wyslouzil, *Phys. Chem. Chem. Phys.*, 2012, **14**, 4505.
22 A. J. Amaya and B. E. Wyslouzil, *J. Chem. Phys.*, 2018, **148**, 085401.
23 A. Bhabhe, H. Pathak and B. E. Wyslouzil, *J. Phys. Chem. A*, 2013, **117**, 5472.
24 D. E. Hagen, R. J. Anderson and J. L. Kassner, Jr., *J. Atmos. Sci.*, 1981, **38**, 1236.
25 H. Laksmono, T. A. McQueen, J. A. Sellberg, N. D. Loh, C. Huang, D. Schlesinger, R. G. Sierra, C. Y. Hampton, D. Nordlund, M. Beye, A. V. Martin, A. Barty, M. M. Seibert, M. Messerschmidt, G. J. Williams, S. Boutet, K. A. Winkel, T. Loerting, L. G. M. Pettersson, M. J. Bogan and A. Nilsson, *J. Phys. Chem. Lett.*, 2015, **6**, 2826.
26 H. Xue, Y. Fu, Y. Lu, D. Hao, K. Li, G. Bai, Z. Ou-Yang, J. Wang and X. Zhou, *J. Am. Chem. Soc.*, 2021, **143**, 13548.
27 K. Ando, M. Arakawa and A. Terasaki, *Chem. Lett.*, 2016, **45**, 961.
28 T. Yoshioka, T. Kusumoto, T. Handa, M. Arakawa and A. Terasaki, *Chem. Lett.*, 2024, **53**, upae222.

29 M. Humar, M. Ravnik, S. Pajk and I. Muševič, *Nat. Photonics*, 2009, **3**, 595.
30 M. Michihata, A. Kawasaki, A. Adachi and Y. Takaya, XXI IMEKO world congress, 2015.
31 R. D. B. Gatherer, R. M. Sayer and J. P. Reid, *Chem. Phys. Lett.*, 2002, **366**, 34.
32 M. Knudsen, *The Kinetic Theory of Gases: Some Modern Aspects*, Methuen Press, 1950.
33 M. Daimon and A. Masumura, *Appl. Opt.*, 2017, **46**, 3811.
34 C. Szegedy, V. Vanhoucke, S. Ioffe, J. Shlens and Z. Wojna, Proceedings of the IEEE conference on CVPR, 2016, p. 2818.
35 G. Brenn and A. Frohn, *Exp. Fluids*, 1993, **15**, 85.
36 L. Rayleigh, *Proc. R. Soc. London*, 1879, **29**, 71.
37 H. Lamb, *Proc. Lond. Math. Soc.*, 1881, **1**, 51.
38 O. A. Basaran, *J. Fluid Mech.*, 1992, **241**, 169.
39 G. Lohöfer, *Int. J. Thermophys.*, 2020, **41**, 30.
40 Y. Sun, H. Muta and Y. Ohishi, *Microgravity Sci. Technol.*, 2021, **33**, 32.
41 F. H. Busse, *J. Fluid Mech.*, 1984, **142**, 1.
42 I. Egry, H. Giffard and S. Schneider, *Meas. Sci. Technol.*, 2005, **16**, 426.
43 *CRC Handbook of Physics and Chemistry*, ed. D. R. Lide, CRC Press, 82nd edn, 2001.
44 P. T. Hacker, *Technical Note 2510*, National Advisory Committee for Aeronautics, 1951.
45 A. Dehaoui, B. Issenmann and F. Caupin, *Proc. Natl. Acad. Sci.*, 2015, **112**, 12020.
46 S. E. Wood, M. B. Baker and B. D. Swanson, *Rev. Sci. Instrum.*, 2002, **73**, 3988.
47 D. M. Murphy and T. Koop, *Q. J. R. Meteorol. Soc.*, 2005, **131**, 1539.
48 D. G. Archer and R. W. Carter, *J. Phys. Chem. B*, 2000, **104**, 8563.
49 D. E. Hare and C. M. Sorensen, *J. Chem. Phys.*, 1987, **87**, 4840.
50 IAPWS, R6-95, 2018, **https://www.iapws.org/relguide/IAPWS-95.html**, access December 2023.
51 M. A. Kazemi, S. H. Zandavi, M. Zargartalebi, D. Sinton and J. A. W. Elliott, *Int. J. Heat Mass Tranf.*, 2023, **204**, 123833.
52 M. L. López and E. E. Ávila, *Geophys. Res. Lett.*, 2012, **39**, L01805.
53 S. Wildeman, S. Sterl, C. Sun and D. Lohse, *Phys. Rev. Lett.*, 2017, **118**, 084101.
54 T. Buttersack and S. Bauerecker, *J. Phys. Chem. B*, 2016, **120**, 504.
55 C. Takahashi, *J. Meteorol. Soc. Jpn.*, 1976, **54**, 448.
56 R. L. Pitter and H. R. Pruppacher, *Q. J. R. Meteorol. Soc.*, 1973, **99**, 540.
57 A. Lauber, A. Kiselev, T. Pander, P. Handmann and T. Leisner, *J. Atmos. Sci.*, 2018, **75**, 2815.
58 P. V. Hobbs and A. J. Alkezweeny, *J. Atmos. Sci.*, 1968, **25**, 881.